JVST A
Journal of Vacuum Science & Technology A

Investigating the magnetic and atomic interface configuration for a model Fe/CrN bilayer system

Cite as: J. Vac. Sci. Technol. A **39**, 063209 (2021); https://doi.org/10.1116/6.0001267
Submitted: 08 July 2021 . Accepted: 01 September 2021 . Published Online: 29 September 2021

Khan Alam, Rodrigo Ponce-Pérez, Kai Sun, et al.

JVST A
Journal of Vacuum Science & Technology A

ARTICLE

avs.scitation.org/journal/jva

Investigating the magnetic and atomic interface configuration for a model Fe/CrN bilayer system

Cite as: J. Vac. Sci. Technol. A 39, 063209 (2021); doi: 10.1116/6.0001267
Submitted: 8 July 2021 · Accepted: 1 September 2021 ·
Published Online: 29 September 2021

Khan Alam,[1] Rodrigo Ponce-Pérez,[2] Kai Sun,[3] Andrew Foley,[4] Noboru Takeuchi,[2] and Arthur R. Smith[4,a)]

AFFILIATIONS

[1]Department of Physics, King Fahd University of Petroleum and Minerals, Dhahran 31261, Saudi Arabia
[2]Centro de Nanociencias y Nanotecnología, Universidad Nacional Autónoma de México, Ensenada, Baja California, Código Postal 22800, Mexico
[3]Department of Materials Science and Engineering, University of Michigan, Ann Arbor, Michigan 48109
[4]Department of Physics and Astronomy, Nanoscale and Quantum Phenomena Institute, Ohio University, Athens, Ohio 45701

[a)]**Electronic mail:** smitha2@ohio.edu

ABSTRACT

A bilayer of iron on chromium nitride (Fe/CrN) is an interesting system for exchange biasing and sensing applications as the Néel temperature of CrN is 280 K and the Curie temperature of Fe is 1043 K. In this paper, we study the crystal and magnetic structures of the Fe/CrN interface at the atomic level. High quality epitaxial Fe/CrN bilayers prepared by molecular beam epitaxy grow in 001 orientation on MgO(001) substrates with uniform layer thicknesses and sharp interfaces. Our data reveal the epitaxial correlation between Fe and CrN crystals and their magnetic structures at the interface. The magnetic anisotropy directions of Fe and CrN are found parallel to $[110]_{MgO}$. We studied the electronic and magnetic properties of the interface by performing the first-principles total-energy calculations. We present a model that combines the crystal and magnetic structures of the Fe/CrN bilayer and fully explains all results.

I. INTRODUCTION

The growth of high quality samples and tuning their properties to meet the increasing demand of information processing with high speed, best accuracy, and high efficiency are the most challenging problems that need to be addressed for advanced technological applications. Reliable growth methods with a high rate of sample reproducibility would be essential for future electronic and spintronic devices. For example, the problem of low efficiency due to poor minority carrier diffusion lengths in photovoltaic cells is often improved by incorporating quantum wells.[1] Similarly, sharp interfaces in bilayer and multilayer systems are critical for exchange biasing and exchange spring effects.[2,3] Nogués *et al.* observed an increase in exchange biasing with a decrease in the interfacial roughness of Fe/FeF_2 bilayers.[4] However, Li *et al.* studied exchange bias as a function of the interfacial roughness in an Fe/FeF_2 bilayer system and observed negligibly small exchange bias for interfaces with zero roughness but observed positive exchange biasing for about 30% roughness and negative exchange biasing for about 50% roughness.[5] The report of Li *et al.* is clearly in contradiction with the report of Nogués *et al.*, which is evidence of the lack of consensus regarding the importance of a sharp interface for exchange biasing.

A bilayer system of iron (Fe) and chromium nitride (CrN) is a potential candidate for sensing applications as it shows interesting exchange biasing and exchange spring effects.[6] CrN is paramagnetic with face centered cubic (FCC) crystal structure at room temperature and goes through magnetostructural transition at 280 K to a low temperature antiferromagnetic phase with orthorhombic crystal structure,[7–9] and concurrently, CrN showed an electronic transition from semiconducting to metallic phase upon cooling;[10] however, Gall's group reported semiconducting properties at low temperatures.[11] Fe is ferromagnetic and metallic with body centered cubic (BCC) crystal structure below 1043 K[12] and retains the same properties at cryogenic temperatures.[13] An Fe/CrN bilayer could be used as a model system for studying the exchange bias and exchange spring effects as its exchange biasing, interfacial coupling, coercivity, and blocking temperature show excellent tunability with Fe and CrN layer thicknesses and stoichiometry.[6,14] Nonuniform crystal growth, interface roughness, and interdiffusion of layers produce intricate magnetic properties, which necessitates

to establish growth parameters and carry out in-depth structural and magnetic analyses.

In this paper, we report the process of growing high quality Fe/CrN bilayer thin films on MgO(001) substrates by molecular beam epitaxy (MBE) and carrying out in-depth structural and magnetic characterizations. We grow continuous layers of Fe and CrN with uniform thicknesses in (001) orientation on MgO(001) substrates. We find that the epitaxial relationship between Fe and CrN is $[100]_{Fe} \parallel [110]_{CrN}$, $[\bar{3}10]_{Fe} \parallel [310]_{CrN}$, and $[110]_{Fe} \parallel [100]_{CrN}$. We report that the magnetic anisotropy directions of Fe and CrN are parallel to $[110]_{MgO}$. We present a model for the Fe/CrN bilayer system that fully explains all results of crystal and magnetic structures.

II. EXPERIMENTAL AND THEORETICAL METHODS

All Fe/CrN bilayer thin films are prepared in a custom designed ultrahigh vacuum thin films growth and characterization facility, which is dedicated to growth and characterization of nitride thin films.[15] The MBE is equipped with custom designed effusion cells for Cr, Fe, and Ga, a quartz crystal thickness monitor, a rf-nitrogen plasma source, and a variable-temperature reflection high energy electron diffraction (RHEED). To ensure high quality epitaxial growth, MgO(001) substrates are first extensively cleaned with acetone followed by isopropyl-alcohol before introducing it into our loadlock, and further cleaned inside the MBE chamber by heating up to 1000 °C during nitrogen plasma flux exposure until RHEED patterns turn streaky. The Cr, Fe, and Ga fluxes are produced with thoroughly degassed effusion cells and calibrated by using a quartz crystal thickness monitor. Nitrogen flux is supplied by a rf-plasma generator, which is calibrated by growing 1×1 stoichiometric GaN, as described in detail elsewhere.[16] CrN layers are grown under nitrogen rich conditions, with the N/Cr flux ratio of 3.9:1 and a substrate temperature of 650 ± 30 °C without any buffer layers. Based on our Rutherford backscattering (RBS) analysis for other CrN films grown under similar conditions published elsewhere,[7] we think that these growth conditions for CrN layers should result in a 1:1 (N:Cr) stoichiometric film. The Fe layer is deposited at room temperature (RT) to prevent alloying of Cr and Fe at the interface. We capped all films with nonmagnetic Ga layer at RT to protect the Fe layer from oxidation when exposed to air for *ex situ* characterizations. The entire growth process is monitored by RHEED and accordingly the growth parameters are adjusted during the film growth.

We determined the *in-plane* crystal orientation of the Fe and CrN layers and their lattice constants by RHEED and used x-ray diffraction (XRD) equipped with a Cu k_α (1.5406 Å) source to determine *out-of-plane* lattice constants and its crystallinity. X-ray reflectometry is employed for finding layer thicknesses and interfacial roughness. Cross-sectional specimens for transmission electron microscopy studies were prepared by *in situ* focused ion beam (FIB) lift-out methods using an FEI Helios 650 SEM/FIB and to protect the surface from the ion beam damage, a carbon layer and then a Pt/C were deposited. A JEOL JEM-2100F field emission gun microscope with a CEOS probe corrector was used that was operated in scanning transmission electron microscopy (STEM) mode. Both high-angle annular dark-field (HAADF) and bright-field images were taken simultaneously. Spin-polarized first-principles total-energy calculations have been employed to investigate the Fe/CrN (001) interface. Calculations were done in the periodic density functional theory framework as implemented in the PWscf code of the Quantum espresso package.[17] Exchange-correlation energies were treated in the local density approximation (LDA) with Perdew–Zunger functional[18] plus Hubbard correction (LDA+U)[19] using the Cococcioni simplified version.[20] Our previous work[9] demonstrated that a value of $U = 4$ eV describes correctly our system. Therefore, we have chosen this value for the calculations. We have used plane waves to expand the valence Khon–Sham states with a cutoff energy of 30 Ry, and Vanderbilt-ultrasoft pseudopotentials in order to treat the core electrons.[21] A supercell method with a surface unit cell with 1×1 periodicity has been used to investigate the interfaces. Each supercell contained 11 CrN monolayers and 9 Fe ML. Since inversion is included, we have two equivalent interfaces in each supercell. The Brillouin zone integration has been done using a Methfessel-Paxton smearing[22] of 0.01 Ry and a special k-points grid of $5 \times 5 \times 1$.[23] We adapted the Interface Formation Energy (IFE) formalism from the work of Guerrero-Sánchez and Takeuchi[24] to investigate the stability of the interfaces. Depth-resolved magnetic profile analyses for the bilayers are carried out using polarized neutron reflectometry (PNR) at the National Institute for Standards and Technology, where the data are acquired after first cooling the sample down to 5 K under an applied magnetic field of 0.7 T along $[100]_{MgO}$. For determining the magnetization anisotropy direction of Fe, we obtained PNR spectra for the remanent magnetization after positive and negative magnetization saturations. To quantitatively understand the depth-dependent magnetization data, we fit it by using REFL1D software.[25,26]

III. RESULTS AND DISCUSSION

We used RHEED to determine the *in-plane* lattice parameters of Fe and CrN layers and their crystallographic relationship and it is known that CrN grows on the MgO(001) substrate in a complete crystallographic registry as $[100]_{CrN} \parallel [100]_{MgO}$, $[310]_{CrN} \parallel [310]_{MgO}$, and $[110]_{CrN} \parallel [110]_{MgO}$.[7] Six RHEED images of a 40 nm thick CrN and 50 nm thick Fe layers recorded at room temperature (RT) are shown in Fig. 1; patterns shown in [(a), (c), and (e)] are related to the CrN layer and patterns shown in [(b), (d), and (f)] are related to the Fe layer. The patterns are also grouped in columns based on the crystallographic directions: $[100]_{CrN}$ (a,b); $[310]_{CrN}$ (c,d); and $[110]_{CrN}$ (e,f). Distinction of these crystallographic directions is their unique streaks spacing. The streak spacing along $[100]_{CrN}$ is smaller than along $[310]_{CrN}$ but larger than along $[110]_{CrN}$ by factors of $\sqrt{\frac{5}{2}}$ and $\sqrt{\frac{1}{2}}$, respectively. Streaks in the top three patterns are labeled with Miller indices based on reciprocal lattice mapping of the CrN lattice.

RHEED images of the CrN layer show sharp streaks indicating high quality epitaxial, single crystal growth, whereas in the RHEED images of the Fe layer show bright spots instead of streaks representing a rough growth. Also, a small fraction of polycrystallinity exists in the Fe layer due to which new spots and few faint Laue rings (L-rings) appeared in the RHEED patterns, but the amount of polycrystallinity is so small that it does not produce any peak in the XRD pattern shown in Fig. 2(a).

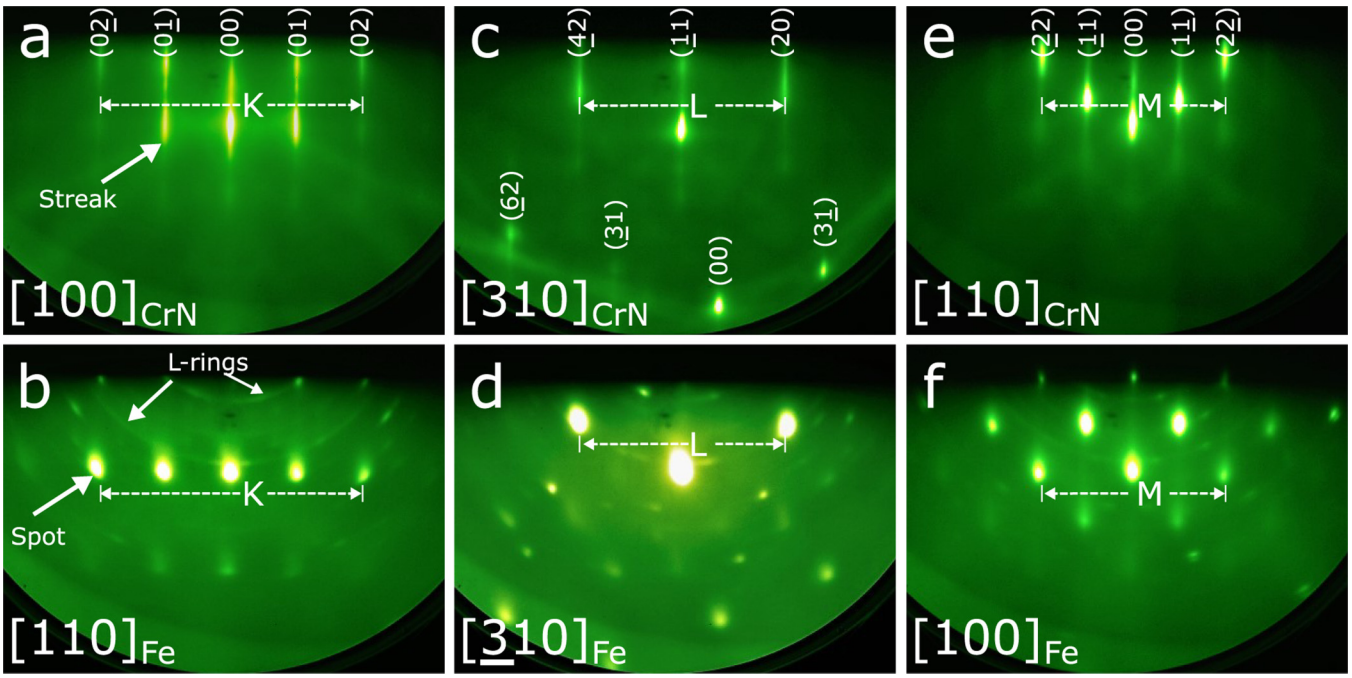

FIG. 1. RHEED patterns of CrN in (a), (c), and (e) along $[100]_{CrN}$, $[310]_{CrN}$, and $[110]_{CrN}$, respectively, show sharp streaks. RHEED patterns of Fe in (b), (d), and (f) along $[100]_{Fe}$, $[\underline{3}10]_{Fe}$, and $[110]_{Fe}$, respectively, show spots with additional faint Laue rings (L-rings).

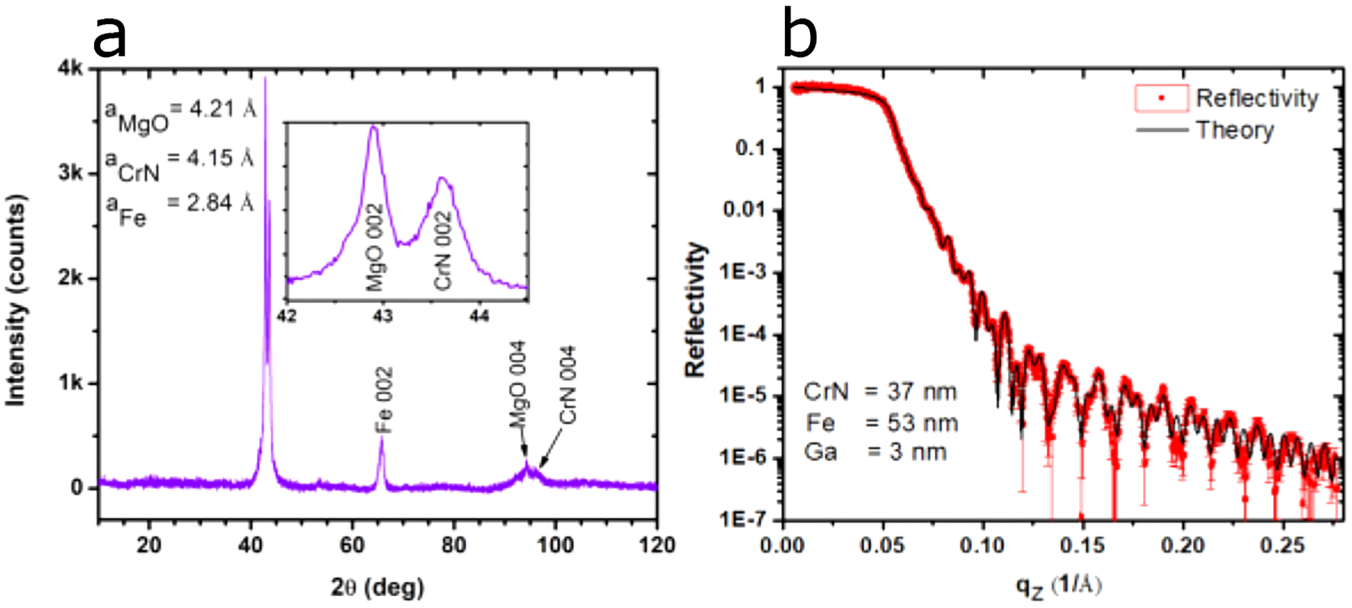

FIG. 2. (a) XRD pattern of Ga/Fe/CrN/MgO(001) multilayer thin film. (b) Red colored squares represent x-ray reflectivity of the film and the black line is a theoretical fit to the data.

RHEED streaks are produced due to the intersection of reciprocal lattice rods with the Ewald sphere[27] and the space between the streaks is inversely proportional to the lattice parameters of the real crystal. The spacing between outer streaks in Fig. 1(a) is represented by K and the same length K is shown in Fig. 1(b); the spacing between the outer streaks for Fe is wider than the CrN streaks, which indicates that the Fe planes in the real Fe lattice are closer together as compared to the CrN planes. It makes sense because 2.87 Å lattice vector of Fe is 2% smaller than the primitive lattice vector of CrN which is 2.93 Å;[6,28] therefore, the first few monolayers of the Fe layer would be under tensile stress and will relax gradually with the layer thickness. Similarly, lengths L and M used along $[310]_{CrN}$ and $[110]_{CrN}$ show an increasing trend in the spacing between Fe streaks. The spacing between two adjacent streaks of Fe and CrN along $[100]_{MgO}$ corresponds to 2.02 ± 0.01 and 2.08 ± 0.01 Å, respectively, which are the same as spacing between (110) planes of Fe and (100) planes of CrN. From the 2.02 ± 0.01 Å interplanar spacing of Fe, we calculate its *in-plane* lattice constant to be $a_{Fe\|} = \sqrt{2} \times 2.02 \pm 0.01$ Å $= 2.86 \pm 0.01$ Å, which is in agreement with 2.87 Å.[6,28] The 2.08 ± 0.01 Å interplanar spacing of CrN gives its *in-plane* lattice constant to be $a_{CrN\|} = 2 \times 2.08 \pm 0.01$ Å $= 4.16 \pm 0.01$ Å, which is in good agreement with 4.16 Å.[7,29,30] Carrying out the same analyses for all RHEED data sets, we found that the epitaxial relationship between Fe and CrN is $[110]_{Fe} \parallel [100]_{CrN}$, $[\bar{3}10]_{Fe} \parallel [310]_{CrN}$, and $[100]_{Fe} \parallel [110]_{CrN}$.

A characteristic θ-2θ XRD pattern of a typical Ga/Fe/CrN/MgO(001) thin film is shown in Fig. 2(a). The scan covers a range of 2θ from 10° to 120°, where three 002 peaks appear, one each for MgO, CrN, and Fe layer is at 2θ = 42.89°, 43.59°, and 65.73°, respectively. Two 004 peaks of MgO and CrN are at 2θ = 93.98° and 95.90°. The inset shows a zoomed-in view of the 002 peaks of MgO and CrN. The 3 nm thick capping layer of Ga does not produce any peak. Using Bragg's equation, the *out-of-plane* lattice constants of MgO and CrN measured to be $a_{MgO\perp} = 4.21 \pm 0.01$ Å and $a_{CrN\perp} = 4.15 \pm 0.01$ Å, which agree with the reported values of 4.21 (Ref. 31) and 4.16 Å,[29] respectively. The *out-of-plane* lattice constant of Fe is measured to be $a_{Fe\perp} = 2.84 \pm 0.01$ Å, which is a little smaller than the reported value of 2.87 Å.[28] The presence of only 002 and 004 peaks of CrN and 002 peak of Fe indicates that the layers grow epitaxially in 001 orientation. The amount of Fe polycrystallinity represented by the faint Laue rings in Figs. 1(b), 1(d), and 1(f) is small and not enough to produce peaks in the XRD pattern.

We measured layer thicknesses and interfacial roughnesses of the thin films by x-ray reflectivity. Reflectivity is the ratio of reflected x-ray intensity to incident x-ray intensity. In Fig. 2(b), solid red colored square symbols plot the reflectivity as a function of momentum transfer (q_z), and the solid black colored line plots the theoretical fit to the data. The total external reflection corresponding to a reflectivity of 1 is below $q_z = 0.02$ Å^{-1}, where the x rays reflect entirely from the top surface without penetrating into the sample. A large fraction of the x rays begin to penetrate into the film around $q_z = 0.05$ Å^{-1} and produce Kiessig fringes. We fit the Kiessig fringes by a detailed theoretical model using PYTHON and REFL1D software[25] to extract structural information. In the model, the fitting parameters are x-ray scattering length density (SLD) for CrN and Fe, interfacial roughness, and layer thicknesses; and all these parameters were allowed to relax in wide ranges. We determined the Ga, Fe, and CrN layer thicknesses are 3 ± 2, 53 ± 2, and 37 ± 2 nm, respectively, which are consistent with the thicknesses determined by STEM images, shown in Fig. 3(a). The interfacial roughness of Ga/Fe and Fe/CrN are found to be 1.7 and 1.4 nm, respectively, both of which fall within one sigma range of their thicknesses determined by the XRR. The Fe/CrN interfacial roughness is equivalent to about seven monolayers, which could be due to the intermixing of the two layers.

A high resolution cross-sectional HAADF image of Fe/CrN thin films at low magnification is shown in Fig. 3(a). All layers are continuous and have uniform thicknesses over the entire range imaged by the STEM. The interface shows high quality crystalline growth for both Fe and CrN layers. The Fe and CrN layers are found to be 52 and 35 nm thick, which are in excellent agreement with the layer thicknesses determined based on the XRR data shown in Fig. 2(b). An atomically resolved bright-field image of Fe and CrN layers taken along $[100]_{MgO}$ is shown in Fig. 3(b). It is interesting to note that the Fe lattice is epitaxial with the CrN lattice and based on our previous studies,[6] we expect the bonding between Fe and N at the Fe/CrN interface, which is supported by our calculations presented in this paper and is in agreement with the model of Shao *et al.*[32]

Lattice constants of the BCC unit cell of Fe and primitive unit cell of CrN are 2.87 and 2.93 Å, respectively, which gives a lattice mismatch of 2.1%. Therefore, a gradient of tensile stress in the Fe layer is expected; more stress near the Fe/CrN interface and a decreasing trend with a distance from the interface. In Fig. 3(b), we observed *in-plane* relaxation of the Fe crystal by counting the number of rows within the length of the two equal distances labeled R37 CrN (37 rows of CrN) and R37.5 Fe (37.5 rows of Fe). More quantitative analyses of the *in-plane* and *out-of-plane* crystal relaxation versus distance from the Fe/CrN interface are presented in Figs. 3(c) and 3(d), respectively. In both figures, the data sets are calibrated based on a CrN lattice constant of 4.15 Å, which corresponds to the interplanar spacing of 2.075 Å. The difference in the charge densities of Fe and CrN produces color contrast in the TEM images. In Fig. 3(b), the CrN layer appears darker than the Fe layer and the interface between the darker and brighter layers is at layer 0. The negative and positive numbers represent the CrN and Fe layers with respect to the interface.

In Fig. 3(c), the data are represented by the blue colored squares connected by linear lines. Due to the lattice mismatch at the interface, the *in-plane* interplanar spacing of CrN is under tensile compression whereas the Fe layer is under tensile strain. The Fe interplanar spacing at the interface is 2.065 ± 0.010 Å and after 34 monolayers, the layer has relaxed by 1.6% to 2.032 ± 0.010 Å. Using the Van der Mervwe model[33] for the layer by layer growth, the critical thickness for the Fe layer is about one monolayer, which is much less than the 34 monolayers; therefore, the misfit dislocations such as edge dislocation may exist on either side of the imaged area, which could partially relieve the coherency strains between the CrN and Fe layers.

In Fig. 3(d), the blue colored squares with error bars show data for the *out-of-plane* interplanar spacing. At the interface, there is an abrupt decrease from CrN to Fe interplanar spacing. There is an increasing trend in the Fe interplanar spacing from layer 5 to

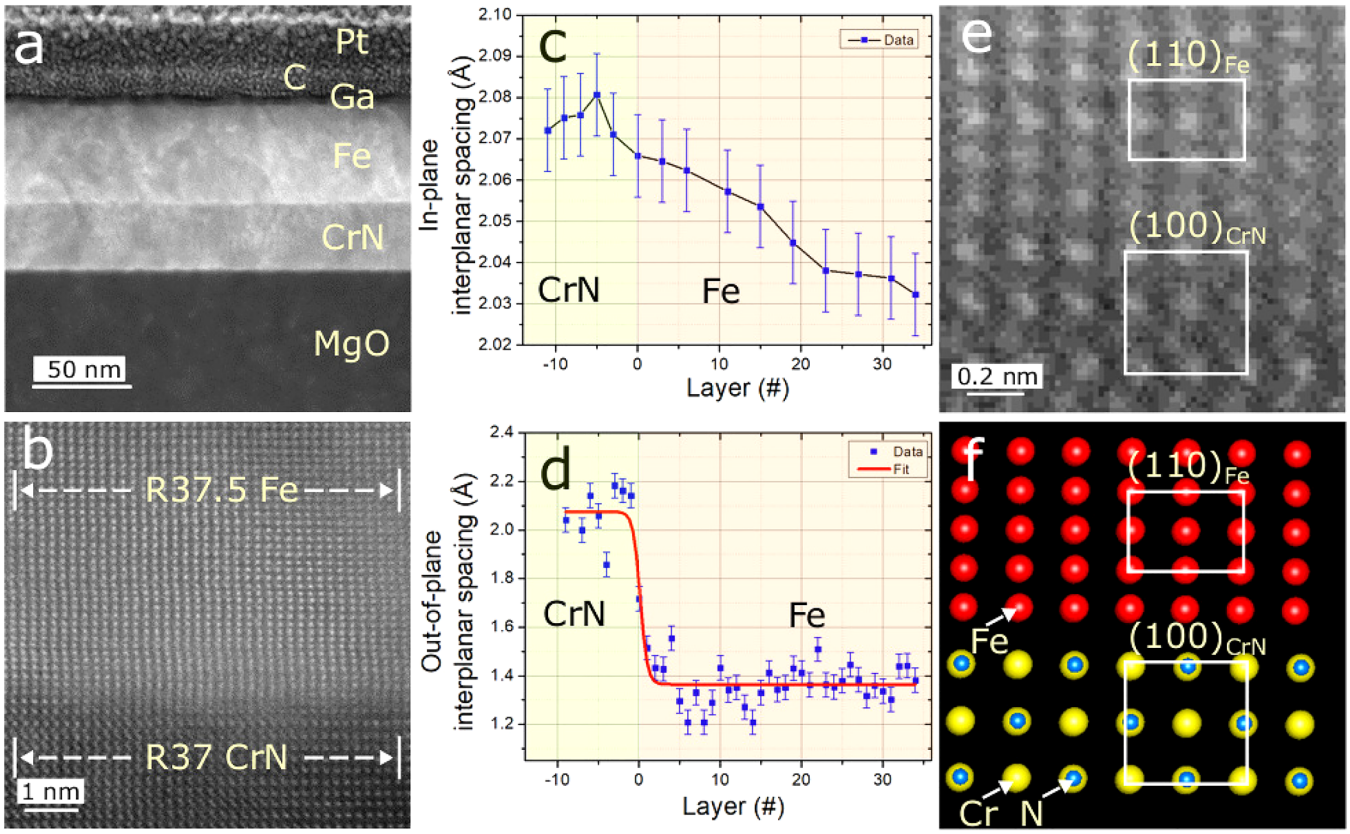

FIG. 3. (a) STEM image of the Ga/Fe/CrN/MgO(001) multilayer thin film. The Pt/C layer is deposited for FIB lift-out preparation. (b) Atomically resolved image of the Fe/CrN interface. (c) *In-plane* and (d) *out-of-plane* interplanar spacings as a function of distance from the interface. (e) Overlays of $(110)_{Fe}$ and $(100)_{CrN}$ planes on an atomically resolved STEM image. (f) The corresponding model for the interface.

layer 34. Due to the *in-plane* tensile strain, the Fe layer is compressed in the *out-of-plane* direction and with more growth, both the *in-plane* tensile strain and *out-of-plane* compression reduce. We also observed the same trend in our models presented in Fig. 4. The data are fitted with the Boltzmann equation $y=A_2+[A_1-A_2]/[1+\exp((x-x_0)/dx)]$, where A_1 and A_2 represent the interplanar spacings of CrN and Fe and x_0 represents the position of the interface. From the fit, we determined that $A_1 = 2.075 \pm 0.033$ Å, $A_2 = 1.365 \pm 0.015$ Å and $x_0 = 0.150 \pm 0.200$ Å. The interplanar spacing of 1.365 ± 0.015 Å corresponds to the lattice constant of 2.730 ± 0.020 Å, which is smaller than the lattice constant determined by XRD.

A zoomed-in view of the Fe/CrN interface is shown in Fig. 3(e) and a possible model is shown in Fig. 3(f), where Fe, Cr, and N atoms are represented by red, golden, and blue colored balls and also labeled in the figure. Based on our RHEED analyses (Fig. 1), we expect that if the electron beam is coming parallel to $[100]_{MgO}$ it would show a projection of the (110) plane for Fe and the (100) plane for CrN, i.e., with the Fe unit cell rotated by 45° with respect to the CrN unit cell. When we analyzed Fig. 3(e) and compared it with the model shown in Fig. 3(f), we found an excellent agreement. Both our RHEED and STEM results are consistent and show that the epitaxial relationship between Fe and CrN is $[110]_{Fe} \parallel [100]_{CrN}$ and $[100]_{Fe} \parallel [110]_{CrN}$.

Taking into account the experimental results, we have simulated different models to describe the interface (see supplementary material[34] for more information), only the three stable models are shown in Fig. 4(b) according to their formation energies [see Fig. 4(a)]. The abscissa shows chemical potential from Cr-rich conditions ($\Delta\mu_{Cr} = 0$ eV) with $\mu_{Cr} = \mu_{Cr}^{bulk}$ and $\mu_N = \mu_{CrN}^{bulk} - \mu_{Cr}^{bulk}$ to Cr-poor conditions ($\Delta\mu_{Cr} = -1.43$ eV) with $\mu_N = \mu_N^{molecule}$ and $\mu_{Cr} = \mu_{CrN}^{bulk} - \mu_N^{molecule}$; and the ordinate shows the variation of the chemical potential from Fe-rich conditions ($\Delta\mu_{Fe} = 0$ eV), where $\mu_{Fe} = \mu_{Fe}^{bulk}$ to Fe-intermediate conditions ($\Delta\mu_{Fe} = -1.00$ eV) with $\mu_{Fe} = \mu_{Fe}^{bulk} - \Delta\mu_{Fe}$. Our calculations show that the epitaxial growth of Fe on the CrN(001) surface is stable under Fe-rich conditions from Cr-rich to Cr-poor conditions. Under these conditions, we found three different interfaces stable. At Cr-poor conditions in the region of chemical potential -1.43 eV $\leq \Delta\mu_{Cr} \leq -1.04$ eV and -0.26 eV $\leq \Delta\mu_{Fe} \leq 0$ eV, we found the formation of a monolayer (ML) of FeN at the interface (FeN model); in the region between

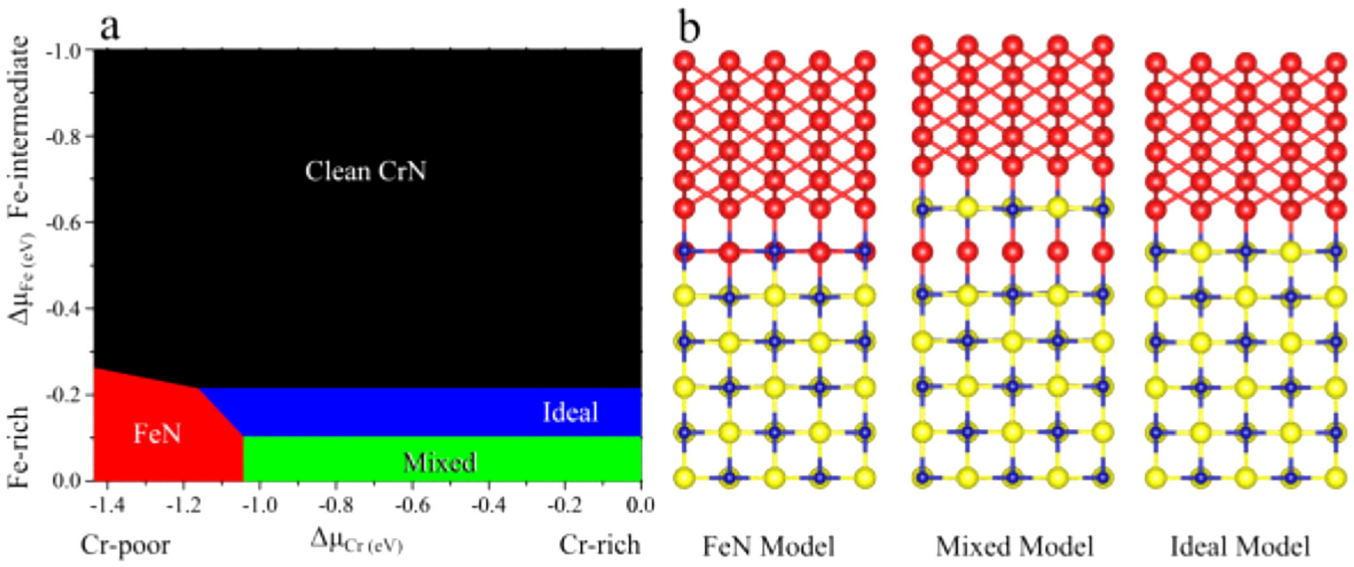

FIG. 4. (a) Phase diagram of the Fe/CrN interface. (b) Three atomistic models of the most stable interfaces according to the interface formation energy formalism.

Cr-intermediate and Cr-rich conditions ($-1.04\,\text{eV} \leq \Delta\mu_{Cr} \leq 0\,\text{eV}$) and Fe-rich conditions ($-0.10\,\text{eV} \leq \Delta\mu_{Fe} \leq 0\,\text{eV}$) the formation of a complex interface (the mixed model) is found to be the most stable. In this configuration, an ML of Fe lies between the first and second ML of CrN, resulting in a Fe/CrN/Fe/CrN stacking. Finally, the formation of an ideal interface (the ideal model) is found to be the most stable from Cr-intermediate to Cr-rich and Fe-rich conditions, in the region $-1.16\,\text{eV} \leq \Delta\mu_{Cr} \leq 0\,\text{eV}$ and $-0.21\,\text{eV} \leq \Delta\mu_{Fe} \leq -0.10\,\text{eV}$.

The atomic models of the three different interfaces are presented in Fig. 4(b). In all cases, the *in-plane* cell parameters of the BCC unit cell of Fe and primitive unit cell of CrN are 2.92 and 2.93 Å ($4.15\text{Å}/\sqrt{2} = 2.93$ Å), respectively.

The FeN model shows a substitution of the Cr atoms of the first CrN ML by Fe atoms, resulting in the formation of a FeN ML at the interface. The *in-plane* Fe-N bond length is 2.07 Å; also, the interplanar distance between the CrN and the FeN monolayer is 2.05 Å and the interplanar distance between the FeN and the Fe ML is 1.93 Å; in both cases, the interplanar distance corresponds with the *out-of-plane* Fe-N bond. The *out-of-plane* bond length for the CrN close to the interface is 2.085 Å and the Fe interplanar distance is 1.35 Å.

For the mixed model, the Fe-N *out-of-plane* bond distance is 1.93 Å for the Fe ML which lies between the first and second CrN monolayers. The *out-of-plane* Fe-N bond distance formed by the first CrN ML and the Fe slab is 1.99 Å. The *in-plane* Cr-N bond distance is 2.07 Å and the *out-of-plane* bond distance close to the interface is of the order of 2.09 Å; also, the Fe interplanar distance close to the interface is 1.38 Å.

In the ideal model, the Fe atoms bond with the N atoms in the top CrN monolayer with a bond length of 1.91 Å. This model has been previously reported by Shao *et al.*[32] as a stable interface, which is in good agreement with our results. For this model, the result is an ideal interface formed by a layer of Fe on top of the most exposed CrN ML where the Fe and CrN regions are easy to distinguish. Close to the interface, the Cr-N *out-of-plane* and *in-plane* bond distances are 2.08 and 2.07 Å, respectively. About the Fe region, the interplanar distance is 1.35 Å. Note that in the three different models, we have a slight contraction in the Fe interplanar distance, which could be attributed to the *in-plane* tensile strain of the Fe atoms close to the interface. For Fe, our experimental value of the *out-of-plane* lattice parameter (2.84 Å) is slightly smaller than in the previous reports (2.87 Å);[28] this reduction in the cell parameter may be due to the *in-plane* tensile strain in the Fe ML close to the interface as determined by the calculations. The *in-plane* and *out-of-plane* interplanar spacings of the three models are in good agreement with the TEM data presented in Fig. 3. Taking this into account, our three stable models could appear in the experiment.

The electronic and magnetic properties of the three stable interfaces are investigated. Figure 5 shows the projected density of states (pDOS) for each layer of the three different models, where only the most important contributions to the DOS are shown. In all cases, the energy reference is the Fermi level and positive and negative values of the DOS correspond to the spin up and down states, respectively. Figure 5(a) displays the pDOS of the ideal model for each of the five layers separately; all layers show metallic behavior. The Fe layers show ferromagnetic (FM) behavior, where the spin up is in majority. The main contribution to the Fe DOS comes from the Fe-3d orbitals. The values of magnetic moments for Fe and Cr in each layer are provided in Table I. Close to the interface, the magnetic moments of the Fe atoms are $2.63\,\mu_B$ and $2.71\,\mu_B$ for the I and II region, respectively. The CrN layer (region III) is antiferromagnetically coupled with the Fe layer.

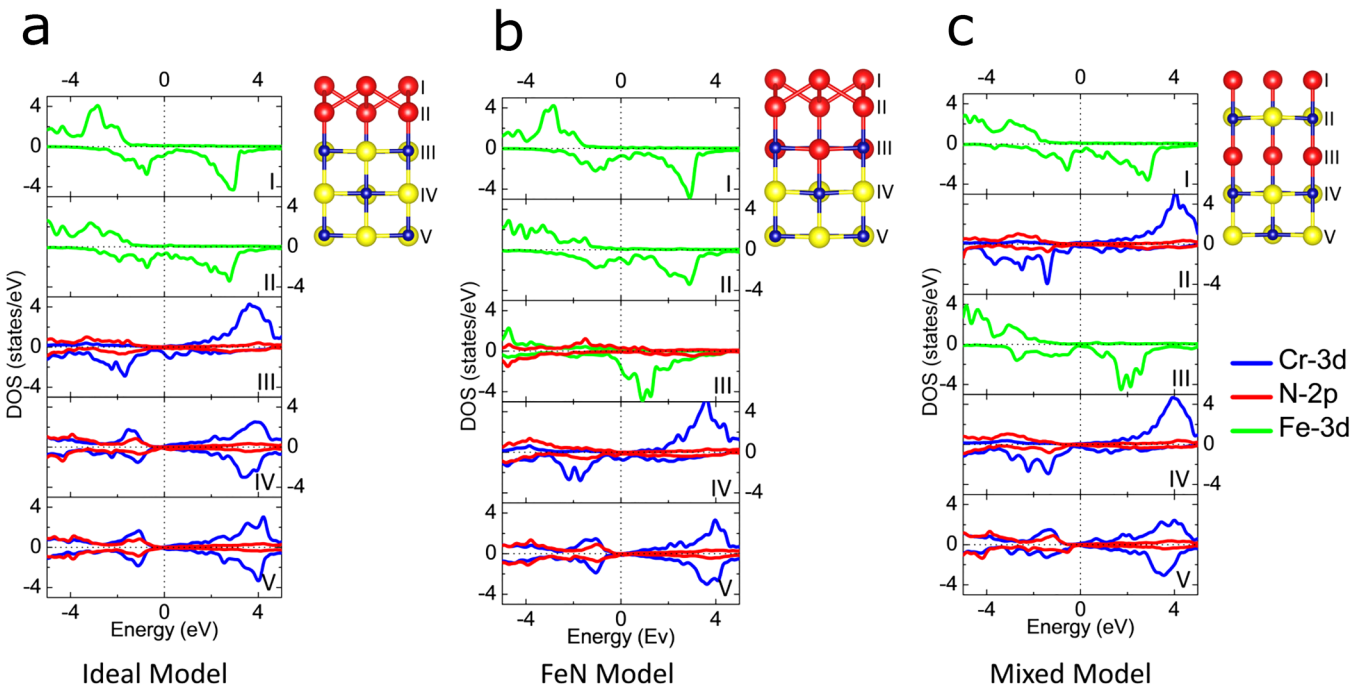

FIG. 5. Projected density of states by layers for (a) ideal, (b) FeN, and (c) mixed models.

Antiferromagnetic (AFM) coupling has also been reported for the interfacial of Fe and Cr layers;[35] this coupling show temperature-driven reversal from paramagnetic to ferromagnetic.[36] The majority spin of region III is down, showing an FM behavior with magnetic moments of $-2.60\,\mu_B$ per Cr atom. At energies below the Fermi level, the main contributions for spin up and spin down DOS come from the N-p and Cr-3d orbitals, respectively. Whereas above the Fermi level, the spin up and spin down DOS consist of the N-p and Cr-3d orbitals. Regions IV and V and inner CrN layers show AFM behavior, which is the low temperature state of the CrN system and magnetic moments per Cr atom are shown in Table I. In the FeN model [Fig. 5(b)], the Fe layer exhibits FM behavior, with spin up as the majority spin. Magnetic moments of Fe in the I and II regions are $2.71\,\mu_B$ and $2.81\,\mu_B$, respectively. The FeN layer (region III) is also FM with Fe magnetic moments of $3.31\,\mu_B$. The FeN layer is coupled ferromagnetically with the Fe layer (region II) and is antiferromagnetically coupled with the CrN layer (region IV). The region IV is ferromagnetic, and region V and inner CrN layers are antiferromagnetic. The DOS for the mixed model is shown in Fig. 5(c), Fe regions (I and III) are FM with spin up as the majority spin, the magnetic moments are of the order of $2.73\,\mu_B$ and $2.65\,\mu_B$, respectively. The intermediate and the lower CrN layers (II and IV) with magnetic moments of $-2.82\,\mu_B$ and $-2.68\,\mu_B$ show FM behavior but with the opposite spin, while the CrN layer (region IV) away from Fe returns to be AFM.

TABLE I. Magnetic moments of Fe and Cr close to the Fe/CrN interface for the three stable models.

Magnetic moment (μ_B/atom) in different regions							
Model	Inner Fe	I	II	III	IV	V	Inner CrN
Ideal	2.65	2.63	2.71	−2.60	±2.59	±2.46	±2.45
FeN	2.70	2.71	2.81	3.31	−2.53	±2.45	±2.45
Mixed	2.68	2.73	−2.82	2.65	−2.68	±2.49	±2.50

Table I summarizes the magnetic moments at the interface. As the calculations demonstrate in all cases, the coupling Fe/Cr is antiferromagnetic. Also, we note that the magnetic moments show a slight increase at the interface. The average magnetic moment for bulk Fe is $2.65\,\mu_B$, while at the interface it is larger than $2.7\,\mu_B$. Fe atoms in inner regions of the Fe slab have average magnetic moments in the range of 2.65–$2.7\,\mu_B$. In the inner CrN region, the average magnetic moment per Cr is $2.45\,\mu_B$, and at the interface they are larger than $2.5\,\mu_B$. The FeN layer exhibits the greatest magnetic moments with values of $3.31\,\mu_B$.

We used PNR to study magnetization at the Fe/CrN interface. PNR provides depth profiles of both the sample structure and its net magnetization. We measured all four cross sections of PNR reflectivity for 37 nm thick CrN and 53 nm thick Fe thin films as shown in Fig. 6(a): two of them are nonspin flip curves R^{++} and R^{--} and the other two are spin-flip curves R^{+-} and R^{-+}. The +/− signs designate whether the neutron spin is parallel/antiparallel to the applied magnetic field and the first/second sign corresponds to the incident/reflected neutrons. The nonspin flip curves contain structural as well as magnetic information, and the difference

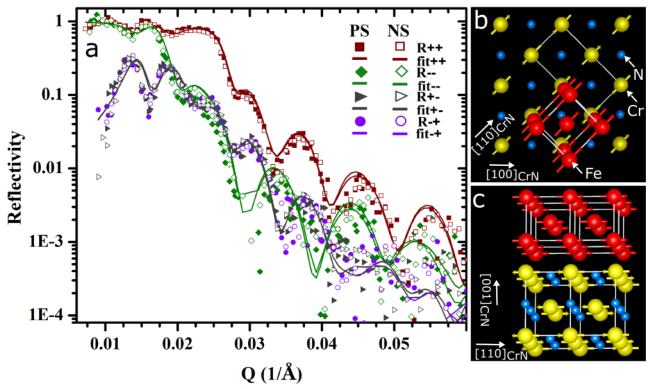

FIG. 6. (a) The PS and NS data, each consists of four spectra R^{++}, R^{+-}, R^{+-}, and R^{+-}. The data obtained after PS and NS are represented by filled and empty symbols, respectively. (b) A top view of Fe/CrN bilayer shows BCC and orthorhombic unit cells of Fe and CrN, respectively. The Cr, N, and Fe atoms are labeled. (c) A 3D model of the bilayer shows two orthorhombic unit cells of CrN and four BCC unit cells of Fe.

between them is due to the parallel component of the net magnetization ($\vec{M}_{\parallel}$) in the sample, whereas the spin-flip curves contain pure magnetic information, and they are sensitive to the perpendicular component of the net magnetization ($\vec{M}_{\perp}$). Based on our vibrating sample magnetometry experiments published elsewhere,[6] we know that +0.7 T and −0.7 T fields should be enough to fully magnetize the sample in positive and negative directions, i.e., positive (PS) and negative saturation (NS), respectively. For performing this experiment, we first cooled down the sample from RT to 5 K under 0.7 T magnetic field applied along $[100]_{CrN}$. To look for remanent magnetization after the PS, we decreased the field to 1.5 mT and measured all four scattering cross sections, which are represented by filled symbols in Fig. 6(a). Similarly, we collected another set of data at 1.0 mT after the NS, which is represented by empty symbols in Fig. 6(a). When we compared the data sets, we find the minor difference between the intensities of the PS and NS data sets, which could be due to the subtle difference in the remanent magnetization after the PS and the NS. But the most important observation is that the R^{+-} and R^{-+} data are at about the same average intensity level as R^{--}, which indicates that a significant fraction of the spins is not parallel to $[100]_{CrN}$ or $[\underline{1}00]_{CrN}$. If the spins were aligned parallel to $[100]_{CrN}$, then the intensities of R^{+-} and R^{-+} would have been significantly lower than the intensity of R^{--} for both PS and NS spectra. To determine the magnetic anisotropy direction of Fe, we used a theoretical model for fitting the neutron reflectivity data using PYTHON and REFL1D.[25] The fitting parameters in the model consisted of remanent magnetization (M_r) of Fe and CrN, the relative angle between the incoming neutron beam and magnetization, neutron SLD for CrN and Fe, interfacial roughness, and layer thicknesses. After initiating these parameters around either their bulk values or the expected values, they were allowed to relax. The model shows that M_r of Fe is 1600 emu/cm^3, which is slightly less than the bulk value of Fe.[37] The Fe spins are found to be *in-plane* at 43 ± 2° with respect to $[100]_{CrN}$ ($[110]_{Fe}$), indicating that the hard axis of magnetization of the Fe layer is parallel to $[100]_{CrN}$ and the easy axis is parallel to $[110]_{CrN}$ ($[100]_{Fe}$). It is established that the Cr spins in CrN are antiferromagnetically ordered in $[110]_{CrN}$[7,8,38] and the easy axis of magnetization for Fe is $[100]_{Fe}$;[39] therefore, the anisotropy directions of both Fe and CrN layers are parallel. These observations are consistent with the crystallographic relationship between Fe and CrN determined by RHEED, XRD, and STEM.

We propose a detailed model for the Fe/CrN bilayers as shown in Figs. 6(b) and 6(c). This model accurately combines the crystal and magnetic structures of the bilayer and fully explains all results. For the clarity of this discussion, we are not showing the CrN layer adjacent to the Fe layer in the ferromagnetic state as predicted by our calculations in Fig. 5. Figure 6(b) shows the top view of the Fe and CrN models, where a BCC unit cell of Fe is shown on top of a monolayer of (001) plane of CrN with an orthorhombic crystal structure. The Cr, N, and Fe atoms are represented by golden, blue, and red colored balls and also labeled in the figure. The spins of Fe and Cr are represented by red and golden colored vectors and can also be identified by the labels in the figure. A 3D view of the model is shown in Fig. 6(c), where four BCC unit cells of the Fe layer are shown on top of the two orthorhombic unit cells of CrN. In the model, the crystallographic relationship between Fe and CrN is $[100]_{Fe} \parallel [110]_{CrN}$, $[\underline{3}10]_{Fe} \parallel [310]_{CrN}$, and $[110]_{Fe} \parallel [100]_{CrN}$. The Cr spins are antiferromagnetically ordered along $[110]_{CrN}$ based on the model of Corliss *et al.*[8,9,40] and Fe spins are ferromagnetically ordered in its easy direction of magnetization[41] $[100]_{Fe}$. Therefore, the magnetic anisotropy directions of both Fe and CrN layers are the same ($[110]_{CrN}$).

IV. CONCLUSIONS

We studied MBE grown Fe/CrN bilayer thin films by various techniques. Based on our experimental results and theoretical calculations, we proposed three models for the Fe/CrN interface that combine the crystal and magnetic structures. An atomically resolved cross section imaged with TEM is the average of many layers, so it cannot accurately determine the interfacial mixing. Similarly, neutron reflectivity averages out the structural and magnetic properties of each layer of the films. We used theoretical calculations to study the electronic and magnetic properties of the interface. We studied tensile and perpendicular strains and compared the *in-plane* and *out-of-plane* lattice constants for the three proposed models and did not find any appreciable difference between them. Therefore, we think that the three proposed models for the interface may coexist. This brings us back to the difficulty in studying the interfaces and accurately quantifying the intermixing of the layers. We suggest that studying the Fe/CrN interface by cross-sectional scanning tunneling microscopy as well as studying a submonolayer Fe layer on the CrN layer by scanning tunneling microscopy techniques can uniquely identify the interfacial model with atomic level precision.

ACKNOWLEDGMENTS

This work was supported by the King Fahd University of Petroleum and Minerals under Award No. SR191024 (STEM image analysis and manuscript preparation) and by the U.S. Department

of Energy, Office of Basic Energy Sciences, Division of Materials Sciences and Engineering under Award No. DE-FG02-06ER46317 (MBE growth, RHEED analysis, and XRD/XRR/PNR analyses). The authors acknowledge Julie Borchers, senior research scientist at the U.S. National Institute of Standards and Technology, for help in acquiring XRR and PNR data at the NIST Center for Neutron Research and for help in the data fitting. R.P.-P. and N.T. thank DGAPA-UNAM (Project Nos. IN110820 and IN101019) and Conacyt (Grant No. A1-S-9070) for partial financial support. Calculations were performed in the DGCTIC-UNAM Supercomputing Center, Project Nos. LANCAD-UNAM-DGTIC-150 and LANCAD-UNAM-DGTIC-51. R.P.-P. acknowledges DGAPA-UNAM for a postdoctoral position.

DATA AVAILABILITY

The data that support the findings of this study are available within the article and its supplementary material.[34]

REFERENCES

[1]G. K. Vijaya, A. Freundlich, D. Tang, and D. J. Smith, J. Vac. Sci. Technol. B **33**, 031209 (2015).
[2]M. Vafaee *et al.*, Appl. Phys. Lett. **108**, 072401 (2016).
[3]M. Perzanowski, A. Zarzycki, J. Gregor-Pawlowski, and M. Marszalek, ACS Appl. Mater. Interfaces **12**, 39926 (2020).
[4]J. Nogués, D. Lederman, T. Moran, I. K. Schuller, and K. Rao, Appl. Phys. Lett. **68**, 3186 (1996).
[5]Y. Li, J.-H. Moon, and K.-J. Lee, J. Magn. **16**, 323 (2011).
[6]K. Alam *et al.*, J. Phys. D: Appl. Phys. **53**, 125001 (2020).
[7]K. Alam *et al.*, Phys. Rev. B **96**, 104433 (2017).
[8]L. Corliss, N. Elliott, and J. Hastings, Phys. Rev. **117**, 929 (1960).
[9]R. Ponce-Pérez, K. Alam, G. H. Cocoletzi, N. Takeuchi, and A. R. Smith, Appl. Surf. Sci. **454**, 350 (2018).
[10]C. Constantin, M. B. Haider, D. Ingram, and A. R. Smith, Appl. Phys. Lett. **85**, 6371 (2004).
[11]M. E. McGahay, B. Wang, J. Shi, and D. Gall, Phys. Rev. B **101**, 205206 (2020).
[12]P. Klugkist and C. Herzig, Phys. Status Solidi A **148**, 413 (1995).
[13]T. N. Rhodin, C. F. Brucker, and A. B. Anderson, J. Phys. Chem. **82**, 894 (1978).
[14]Y. Tsuchiya, K. Kosuge, S. Yamaguchi, and N. Nakayama, Mater. Trans. JIM **38**, 91 (1997).
[15]W. Lin *et al.*, Rev. Sci. Instrum. **85**, 043702 (2014).
[16]K. Alam, A. Foley, and A. R. Smith, Nano Lett. **15**, 2079 (2015).
[17]P. Giannozzi *et al.*, J. Phys.: Condens. Matter **21**, 395502 (2009).
[18]J. P. Perdew and A. Zunger, Phys. Rev. B **23**, 5048 (1981).
[19]V. I. Anisimov, F. Aryasetiawan, and A. Lichtenstein, J. Phys.: Condens. Matter **9**, 767 (1997).
[20]M. Cococcioni and S. De Gironcoli, Phys. Rev. B **71**, 035105 (2005).
[21]D. Vanderbilt, Phys. Rev. B **41**, 7892 (1990).
[22]M. Methfessel and A. Paxton, Phys. Rev. B **40**, 3616 (1989).
[23]H. J. Monkhorst and J. D. Pack, Phys. Rev. B **13**, 5188 (1976).
[24]J. Guerrero-Sánchez and N. Takeuchi, Comput. Mater. Sci. **144**, 294 (2018).
[25]P. A. Kienzle, J. Krycka, N. Patel, and I. Sahin, Refl1d (version 0.7.7), 2011, see http://reflectometry.org/danse (accessed February 28, 2016).
[26]Certain commercial equipment, instruments, or materials (or suppliers, or software, etc.) are identified in this paper to foster understanding. Such identification does not imply recommendation or endorsement by the National Institute of Standards and Technology, nor does it imply that the materials or equipment identified are necessarily the best available for the purpose, 2021.
[27]J. E. Mahan, K. M. Geib, G. Robinson, and R. G. Long, J. Vac. Sci. Technol. A **8**, 3692 (1990).
[28]K. Hermann, *Crystallography and Surface Structure: An Introduction for Surface Scientists and Nanoscientists* (Wiley, New York, 2011).
[29]Y. Liu *et al.*, Thin Solid Films **520**, 90 (2011).
[30]C. Real, M. A. Roldan, M. D. Alcala, and A. Ortega, J. Am. Ceram. Soc. **90**, 3085 (2007).
[31]M. P. Marder, *Condensed Matter Physics* (Wiley, New York, 2010).
[32]W. Shao *et al.*, J. Alloys Compd. **810**, 151921 (2019).
[33]A. Kumar and A. Subramaniam, Appl. Surf. Sci. **275**, 60 (2013).
[34]See the supplementary material at https://aip.scitation.org/doi/suppl/10.1116/6.0001267 for different simulated models for the Fe/CrN interface.
[35]K.-Y. Kim *et al.*, Phys. Status Solidi B **244**, 4499 (2007).
[36]S. R. Ali *et al.*, Phys. Rev. B **82**, 020402 (2010).
[37]B. D. Cullity and C. D. Graham, *Introduction to Magnetic Materials* (Wiley, New York, 2011).
[38]K. Inumaru, K. Koyama, N. Imo-Oka, and S. Yamanaka, Phys. Rev. B **75**, 054416 (2007).
[39]Y. Park, E. E. Fullerton, and S. Bader, Appl. Phys. Lett. **66**, 2140 (1995).
[40]A. Filippetti and N. A. Hill, Phys. Rev. Lett. **85**, 5166 (2000).
[41]C. Kittel and P. McEuen, *Introduction to Solid State Physics* (Wiley, New York, 1976), Vol. 8.